PCCP

PAPER

View Article Online
View Journal

Cite this: DOI: 10.1039/c6cp01100d

CO oxidation by MoS_2-supported Au_{19} nanoparticles: effects of vacancy formation and tensile strain†

Soonho Kwon,[a] Kihyun Shin,[a] Kihoon Bang,[a] Hyun You Kim[b] and Hyuck Mo Lee*[a]

Received 18th February 2016,
Accepted 10th April 2016

DOI: 10.1039/c6cp01100d

www.rsc.org/pccp

The mechanism of the catalytic oxidation of CO activated by MoS_2-supported Au_{19} nanoparticles (NPs) was studied using density functional theory calculations. Of particular interest were the effects of the physical/chemical modification of a MoS_2 support on the CO oxidation pathway and the activation of specific reactive centers, *i.e.*, the Au atoms of Au_{19} or the Au–MoS_2 perimeter sites. We systematically modified MoS_2 by introducing an S vacancy or 5% tensile strain and studied the shift of each reaction step and the overall change in the reaction pathway and activity. Despite the lack of direct involvement of the Au–MoS_2 perimeter in the reaction, the combination of an S vacancy and the tensile strain in the MoS_2 support was found to improve the stability and catalytic activity of Au NPs for CO oxidation. The results show that support modification can provide information for new pathways for the rational design of Au-based catalysts.

1 Introduction

Au nanoparticles (NPs) have attracted great interest because of their unusual catalytic activities at the nanoscale toward CO oxidation.[1,2] Because small Au NPs are inevitably structurally volatile, the use of a robust support material, such as a mesoporous oxide architecture, is essential for the design of catalysts for industrial applications. However, from the perspective of catalysis design, the incorporation of a support material opens up new opportunities for catalyst design through the formation of the interface.[3] For example, recent findings regarding the role of Au-support interfaces in CO oxidation show that the perimeter activates oxygen, and furthermore, the findings have provided fundamental insights into the chemical nature of the reactive species of the supported Au catalysts.[4–6] In this respect, optimization of the Au-support interface may cause new chemical properties to emerge that could enable intensive rational catalyst design beyond just a simple modification of the composition and shape of the Au NPs.

The unique mechanical, chemical, optical, and electronic properties[7–10] of two-dimensional (2D) layered transition metal dichalcogenides (TMDs) have accelerated their utilization in a wide range of applications, such as Li-ion batteries,[11–14] phototransistors,[15–17] field-effect transistors,[18–20] memory devices,[21,22] and gas sensors.[22–24] Regarding the TMDs, MoS_2 is a widely used catalyst in hydrodesulfidation (HDS) in the oil refining industry. Recently, it has been of intense interest as a catalyst for the evolution of hydrogen.[25–30] Moreover, modified (exfoliated) MoS_2 can also be a supporting template for the epitaxial growth of noble metal nanostructures.[31] Metal–MoS_2 hybrid systems, such as metal nanoparticles (NPs) supported on MoS_2, have demonstrated great potential for the catalytic splitting of water,[32] hydrazine oxidation,[33,34] and for methanol oxidation.[35,36] Such an interesting catalytic usefulness of MoS_2 presumably originates from its versatile electronic structure, which can undergo direct-to-indirect gap transition by changing the number of layers and an insulator-metallic transition by applying a strain or an electric field.[35,37–39] In particular, the Au NP/MoS_2 NP system has recently been investigated as an oxygen reduction reaction (ORR) catalyst and was found to exhibit better performance than that of commercial Pt/C in alkaline media.[40] These results imply that the synergistic effect between Au and MoS_2 can bring about an unexpected catalytic activity, as has also been reported by Su *et al.* for electrochemical biosensing.[41] Above all, it demonstrated catalytic activity for CO conversion for a solid oxide fuel cell (SOFC) using H_2S-containing syngas, which implies that Au/MoS_2 can be a good candidate as a catalyst for CO oxidation, as the authors indicated.[42]

Herein, we employed MoS_2 as a supporting material for Au_{19} NPs and studied the mechanism of CO oxidation catalyzed by the MoS_2-supported Au_{19} NPs (Au_{19}/MoS_2) using density

[a] Department of Materials Science and Engineering, KAIST, 291 Daehak-ro, Yuseong-gu, Daejeon 34141, Republic of Korea. E-mail: hmlee@kaist.ac.kr
[b] Department of Materials Science and Engineering, Chungnam National University, 99 Daehak-ro, Yuseong-gu, Daejeon 34134, Republic of Korea

† Electronic supplementary information (ESI) available. See DOI: 10.1039/c6cp01100d

functional theory (DFT) calculations. Because the activity of CO oxidation catalyzed by the supported Au clusters is strongly influenced by the defects[43–45] or strain[46] in the support materials, we considered the effect of these surface modifications in our system. The corresponding changes in the electronic interaction between Au and MoS_2 and the catalytic activity induced by the formation of vacancies and tensile elongation were studied. We found that surface modifications of the MoS_2 support can induce large differences in the molecular adsorption of CO and O_2 on Au_{19}/MoS_2 and thus the overall catalytic activity of CO oxidation. Our findings provide a fundamental understanding of the use of TMDs as a tuneable supporting material for metal NPs.

2 Computational methods

All DFT calculations were performed using the Vienna *ab initio* simulation package (VASP) code.[47,48] Electron exchange and correlation were treated within the generalized gradient approximation (GGA)[49] in the form of the Perdew–Wang (PW91) functional.[50] The interaction between the ionic core and the valence electrons was described by the projector-augmented wave method[51] and involved the valence electrons with a plane-wave basis up to an energy cut-off of 400 eV. The Brillouin zone was sampled at the Γ point. The convergence criteria for the electronic structure and the atomic geometry were 10^{-4} eV and 0.01 eV Å^{-1}, respectively. The climbing image nudged elastic band (CI-NEB) method[52] developed by Henkelman and Jónsson was used to calculate the reaction barrier by discretizing the reaction path with eight images. The support was described with a 6×6 MoS_2 monolayer with 20 Å of vacuum.

Gruene *et al.* investigated[53] neutral gold NPs/clusters in the gas phase using vibrational spectroscopy, and found the C_{3v} structure of Au_{19} to be a minimum, as had been accurately predicted by the DFT calculations.[54] Experimental studies showed that quasi-triangular crystalline Au NPs can grow on the MoS_2(0001) plane in a Volmer–Weber mode[55] and that the surface plane of MoS_2 serves as a growth template for Au NPs along its (111) plane; furthermore, the defects on the basal plane of MoS_2 can effectively attract Au precursors (clusters) and serve as nucleation sites.[56] Based on previous studies, we adapted a truncated pyramidal Au_{19} NP structure as reported by Gruene *et al.*[53] and supported it on the MoS_2(0001) plane (Au_{19}/MoS_2). Also, we excluded a system containing isolated Au atoms,[57] because it was observed that single Au atoms can easily diffuse on a MoS_2 surface, and the diffusion barrier can be as low as $\sim$40 meV, as shown by DFT calculations.[58]

Generally, vacancies[43–45] and strain[46] on the support significantly affect the catalytic activity of NPs. Therefore, we introduced four model systems depending on the existence of an S vacancy (a defect) and the tensile strain (5%, strained) in the MoS_2 support (refer to Table 1). Bertolazzi *et al.*[59] found that the critical tensile strain of failure of a MoS_2 monolayer was approximately 0.06–0.11 by assuming a linear stress–strain relationship. Also, the findings of other theoretical studies[60,61] are in good agreement with the experimental data. Thus, we speculated that a 5% tensile strain does not lead to a breaking of the MoS_2 layer but is sufficient to study the effect of the strain. Additionally, because the formation energy of the Mo-related defects is high (>4 eV), we considered only an S vacancy, which can also act as an electron trapping center.[62] An S vacancy was generated below the central gold atom of the bottom layer of the Au_{19} particle (refer to Fig. 1a and Fig. S1, ESI† for the geometries).

Table 1 The four studied Au_{19}/MoS_2 systems, indicating the modification of the MoS_2 support

System	No vacancy	1 vacancy
No strain (0%)	Non-modified (N)	Defective (D)
5% tensile (5%)	Strained (S)	Defective and strained (DS)

The binding energy $\left(E_{\text{bind}}^{\text{Au}_{19}}\right)$ of the Au_{19} NP on the MoS_2 support was defined as

$$E_{\text{bind}}^{\text{Au}_{19}} = E_{\text{Au}_{19}/\text{MoS}_2} - \left[E_{\text{Au}_{19}} + E_{\text{MoS}_2}\right]$$

where $E_{\text{Au}_{19}/\text{MoS}_2}$ is the total energy of Au_{19}/MoS_2 and $E_{\text{Au}_{19}}$ and E_{MoS_2} are the energies of a free-standing Au_{19} NP and a MoS_2 single layer, respectively.

The molecular adsorption energy of CO ($E_{\text{ads}}^{\text{CO}}$) and O_2 ($E_{\text{ads}}^{\text{O}_2}$) was systematically studied (Fig. S2, ESI†), and the corresponding energy was defined as

$$E_{\text{ads}}^{\text{molecule}} = E_{\text{molecule}/\text{Au}_{19}/\text{MoS}_2} - \left[E_{\text{molecule}} + E_{\text{Au}_{19}/\text{MoS}_2}\right]$$

where $E_{\text{molecule}/\text{Au}_{19}/\text{MoS}_2}$ is the total energy of Au_{19/MoS_2} with CO or O_2 and E_{molecule} is the energy of a free-standing molecule.

3 Results and discussion

3.1 The interaction between the Au_{19} NPs and the MoS_2 support

During the geometry optimization, the relaxed pyramidal Au_{19} NPs on the MoS_2 support did not exhibit any significant deformation. Density functional molecular dynamics (DFT-MD) for $\sim$6.5 ps at 300 K also supports this aspect (please see the attached video (Au19_MoS2_6.5 ps.avi), ESI†). For further analyses, we categorized the Au_{19} NPs into three geometric layers: top, middle, and bottom (Fig. 1a). The location of each Au atom of the bottom layer of Au_{19} NPs was well matched with the S atom immediately beneath it (Fig. S1, ESI†) as in a previous experiment.[63]

To investigate how the modification of the support affects the Au_{19}–MoS_2 interaction, we calculated the $E_{\text{bind}}^{\text{Au}_{19}}$ for all the systems described above. We found that the adsorption energy increases when an S vacancy is formed or when a strain is applied (Table 2). The Au_{19} NP is bound to the intact MoS_2 support with an $E_{\text{bind}}^{\text{Au}_{19}}$ of -1.65 eV. The $E_{\text{bind}}^{\text{Au}_{19}}$ increases by 27%, 64%, and 70% for the Au_{19}/MoS_2-D, Au_{19}/MoS_2-S, and Au_{19}/MoS_2-DS systems, respectively. Clearly, the vacancy strengthens the Au–MoS_2 interaction. However, a more prominent effect was found in the systems with a strained MoS_2 support (Fig. 2). Vacancy formation has been considered as a typical strategy for the minimization of coalescence

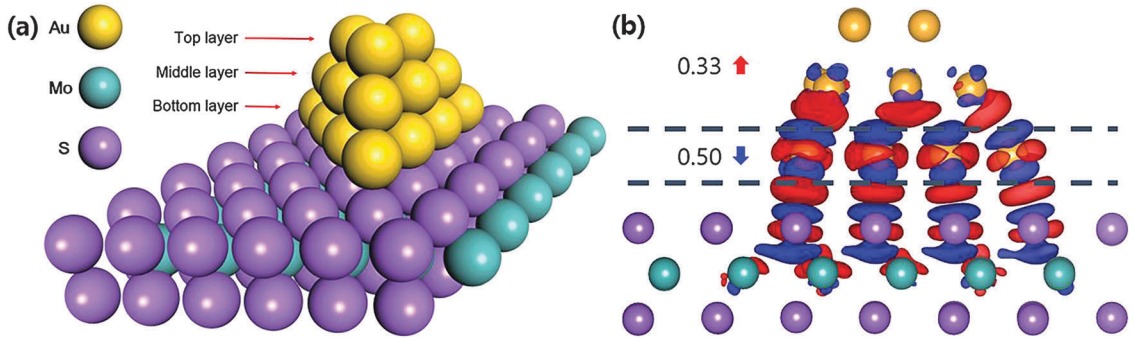

Fig. 1 Morphology of Au_{19}/MoS_2 (a): geometric configuration of the Au_{19}/MoS_2-N system. The yellow, cyan, and purple balls represent the Au, Mo, and S atoms, respectively. The top, middle, and bottom layers are indicated. (b): Au_{19} deposition-induced charge redistribution in the Au_{19}/MoS_2 system. The red and blue regions represent electron accumulation and depletion, respectively. The isosurface value is 0.001 e $Bohr^{-3}$.

Table 2 Calculated binding energy of Au_{19} NPs on MoS_2 supports $\left(E_{bind}^{Au_{19}}\right)$, the amount of charge transfer from Au_{19} to MoS_2 calculated by Bader charge analysis, and the average distance between the sulfur atoms of MoS_2 and the bottom layer of Au_{19} (d_{S-B})

	Au_{19}/MoS_2-N	Au_{19}/MoS_2-D	Au_{19}/MoS_2-S	Au_{19}/MoS_2-DS
$E_{bind}^{Au_{19}}$	−1.65 eV	−2.10 eV	−2.71 eV	−2.80 eV
Charge transfer[a]	−0.17 e	−0.38 e	−0.38 e	−0.43 e
d_{S-B}	2.63 Å	2.53 Å	2.45 Å	2.42 Å

[a] A negative value indicates that the Au_{19} NP has lost the corresponding amount of electron density.

of NPs because the vacancy strongly binds the Au NPs. Moreover, our results show that an applied tensile strain on MoS_2 can also significantly stabilize the NPs, even more than the S vacancy does.

A Bader charge analysis[64,65] has shown that the MoS_2 draws electron density from the supported Au_{19} NPs, making the Au_{19} positively charged (Table 2). In the stoichiometric non-strained system, for an Au_{19}/MoS_2-N, only 0.17 e of electron density is transferred from the Au_{19} to the MoS_2. However, when either an S vacancy is formed or a 5% tensile strain is applied, an almost equivalent amount of electron density is transferred (0.38 e) from the Au_{19} to the MoS_2. This is more than double the value for the Au_{19}/MoS_2-N. The average distance between the sulfur atoms and the bottom layer of the Au_{19} (d_{S-B}) decreases with the degree of modification of the support.

The charge density difference (CDD) in Fig. 1b shows that the charge redistribution upon the deposition of the Au_{19} mainly occurs in the interface region and that the Mo atoms in the MoS_2 support are also strongly involved. A quantitative analysis of the Au_{19}/MoS_2-N system demonstrated that the bottom layer of the Au_{19} NPs loses a significant amount of electron density (0.50 e), and, in contrast, the middle and top layers gain 0.20 e and 0.13 e, respectively. The Mo atoms below the Au_{19} also gained a total of 0.18 e. The net amount of decrease in the electron density of the S atoms is marginal (a total 0.01 e to the S atoms). The analysis shows that upon the deposition of Au_{19} on MoS_2, the upper Au layers acquire extra electron density, whereas the contact layer (bottom layer) loses electron density. In other systems, the electronic interaction between the particle and the support is stronger than that of the bare system, as expected from the Bader charge analysis and adsorption energies. (Fig. S3, ESI†)

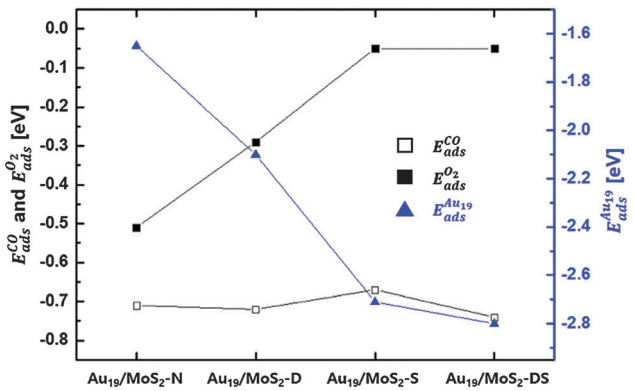

Fig. 2 Trends in the Au_{19}–MoS_2 interaction and CO and O_2 adsorption over the studied systems. Defective or/and strained MoS_2 supports more strongly bind Au_{19} NPs. The energy of CO adsorption on Au_{19}, E_{ads}^{CO}, varies within ±0.05 eV in all the studied systems, whereas the energy of O_2 adsorption, $E_{ads}^{O_2}$, is significantly low in the systems with defective or/and strained MoS_2.

3.2 CO and O_2 adsorption on the Au_{19}–MoS_2 support

The adsorption of CO and O_2 is an initial step for the facile oxidation of CO. To find the preferred binding sites, we systematically studied the adsorption behaviors of CO and O_2 on the Au NPs of four different Au_{19}/MoS_2 systems and the interface between the Au NPs and their support in the Au_{19}/MoS_2-N system. The most stable adsorption of CO and O_2 occurs on the top layer of the Au_{19} NPs, in agreement with previous reports.[66–69] The stable adsorption configurations are shown in Fig. S4 (ESI†). CO preferentially adsorbs on one Au atom of the top layer with an E_{ads}^{CO} of −0.71 eV (Fig. S4a, ESI†). The most stable adsorption site for O_2 is the top-hollow-bridge (THB) site of the top layer (Fig. S4b, ESI†) with an $E_{ads}^{O_2}$ of −0.51 eV.

The $E_{ads}^{O_2}$ is significantly affected by modifying the MoS_2 support compared to the case of E_{ads}^{CO}, as shown in Fig. 2, even though the local atomic coordination is unchanged.[70] Additionally, the $E_{ads}^{O_2}$ is

almost inversely proportional to the $E_{bind}^{Au_{19}}$, implying that O_2 adsorption is closely related to the strength of the Au_{19}–MoS_2 interaction. As the Au_{19} NPs strongly interact with the MoS_2 support, they share more electrons in the Au–MoS_2 interaction rather than saving them for subsequent O_2 adsorption. Such behavior has been discussed in the previous section with the results of the Bader charge analysis. The most significant effects were observed in the Au_{19}/MoS_2-S and Au_{19}/MoS_2-DS systems. These results suggest that the energetics of O_2 adsorption on Au NPs supported on a MoS_2-like two-dimensional TMD support could be easily modulated by applying a mechanical force to the support.

3.3 Bimolecular CO oxidation on Au_{19}/MoS_2

Because our Au/MoS_2 system cannot oxidize CO through the Mars–van Krevelen mechanism, the coadsorption of CO and O_2 is required to activate the Langmuir–Hinshelwood (LH) type of CO oxidation pathway. The most favorable CO–O_2 coadsorption configuration in the Au_{19}/MoS_2-N system is presented in Fig. S5 (ESI†). Following the initial adsorption of CO, a subsequent O_2 adsorption occurs on the THB site with an $E_{ads}^{O_2}$ of −0.58 eV. The pathway for CO oxidation by the bimolecular LH mechanism for all systems is shown in Fig. 3. Because the second half of the CO oxidation is catalyzed by the Au NPs, the oxidation of CO by the remnant O* on the Au NPs, is relatively faster than the first half of the CO oxidation, which requires the activation and dissociation of O_2. We thus considered the first half of the reaction to estimate the CO oxidation activity.

Table 3 shows the E_{ads}^{CO} and $E_{ads}^{O_2}$ of CO–O_2 coadsorption, the activation energy barriers for OCOO* formation and CO_2 production, and the maximum reaction rates for each system at T = 298 K, P(CO) = 0.01 bar and $P(O_2)$ = 0.21 bar. Details of the microkinetic analysis are given in the ESI.† Compared to the cases of single O_2 adsorption, the presence of the pre-bound CO increases the value of $E_{ads}^{O_2}$ in all the Au_{19}/MoS_2 systems. In particular, in the Au_{19}/MoS_2-DS system, $E_{ads}^{O_2}$ increased by 0.28 eV, implying that it is possible to control the interaction between the CO and O_2 molecules through modification of the MoS_2 support. Of all the studied systems, the Au_{19}/MoS_2-N exhibited the highest reaction rate (2.3×10^3 s^{-1}). Remarkably, the reaction rate can differ by seven orders of magnitude depending on the support conditions. Note that the CO oxidation was activated by the same reaction center and the reaction pathway was not changed. The results show that the chemical or physical state of a supporting material can substantially affect the overall CO oxidation rate, even though the supporting material is not directly involved in the reaction.

Table 3 Microkinetic analysis of CO oxidation by the bimolecular LH mechanism[a]

System	E_{ads}^{CO}	$E_{ads}^{O_2}$	TS1+	TS1−	TS2+	Rate (s^{-1})
Au_{19}/MoS_2-N	−0.71	−0.58	0.21	0.13	0.41	2.3×10^3
Au_{19}/MoS_2-D	−0.72	−0.45	0.28	0.05	0.39	4.1×10^{-2}
Au_{19}/MoS_2-S	−0.67	−0.17	0.16	0.06	0.26	1.6×10^{-1}
Au_{19}/MoS_2-DS	−0.74	−0.33	0.25	0.06	0.41	4.6×10^{-4}

[a] Energy values are presented in eV.

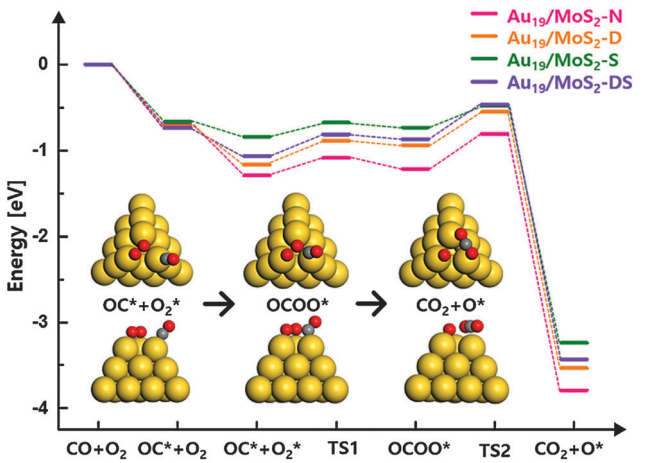

Fig. 3 Calculated CO oxidation pathway on Au_{19}/MoS_2 systems by the bimolecular LH mechanism.

The TS2, the activation energy for CO_2 production from the OCOO* reaction intermediate, is the rate-determining step for CO oxidation. However, the formation of the OCOO* intermediate from the coadsorbed CO and O_2 is energetically uphill. Although the TS1 is considerably low, to assure the high rate of the forward reaction (CO + O_2 → OCOO*), the rate of the reverse reaction (OCOO* → CO + O_2) would exceed that of the forward reaction. Therefore, the short lifespan of the OCOO* reaction intermediate leads to a low surface concentration of the OCOO* intermediate, which negatively attributes to the overall rate. However, from the point of view of catalysis design, the chemical stability of the OCOO* reaction intermediate is exquisitely balanced between the TS2 and the reverse activation barrier of TS1. Although one can extra-stabilize the OCOO* intermediate and turn its formation exothermic, in this situation the TS2 would increase accordingly and thus the rate would decrease.

The experimental results of the deposition of Au on MoS_2 show that the Au NPs were hardly stabilized on a stoichiometrically clean MoS_2 plane. In contrast, the Au NPs were found to be well deposited at the defect sites on the chemically exfoliated MoS_2 supports.[56,71–74] Presumably, although the Au_{19}/MoS_2-N system showed the highest reaction rate, the oxidation of CO by the association of single CO and O_2 molecules can hardly occur.

3.4 Trimolecular CO oxidation on Au_{19}/MoS_2

Under practical conditions for CO oxidation, the catalyst can bind more than one of the reacting molecules. As presented in the previous section, we found that the pre-adsorbed CO strengthens the binding of O_2. This effect can be further emphasized as the Au_{19} binds more CO molecules together with O_2. Previously, Zeng and coworkers[68] reported that such a type of double CO-assisted activation of O_2 and bond breaking (CO self-promoting oxidation) occurs on the triangular Au_3 motif. Because the triangular Au_3 motif was the reaction center of our Au_{19}/MoS_2 system, we also examined CO oxidation by the trimolecular LH mechanism (Fig. 4).

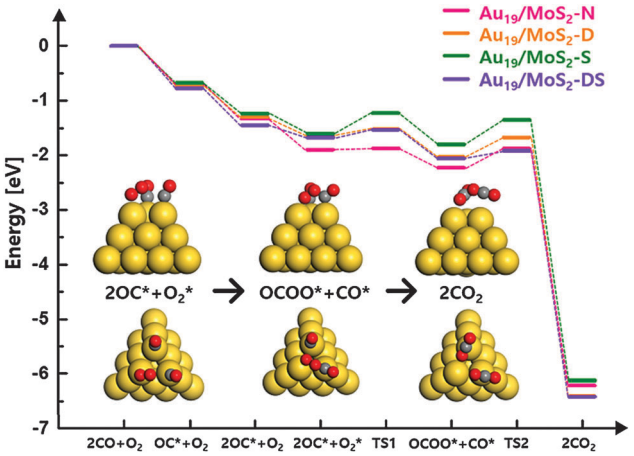

Fig. 4 Calculated CO oxidation pathway on Au_{19}/MoS_2 systems by the trimolecular LH mechanism.

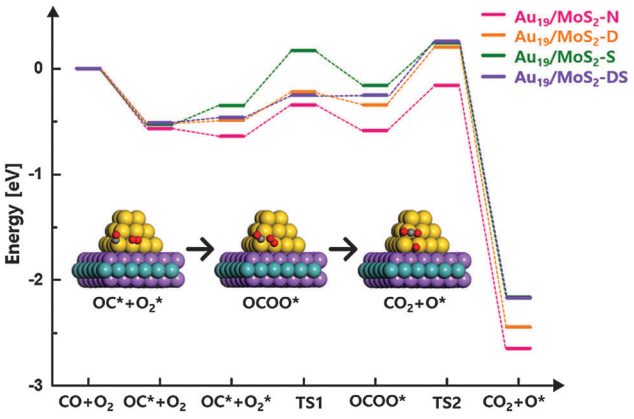

Fig. 5 Calculated CO oxidation pathway at the perimeter near the interface between the Au_{19} NP and the MoS_2 support.

Table 4 Microkinetic analysis of CO oxidation by the trimolecular LH mechanism[a]

System	$E_{ads}^{CO^1}$	$E_{ads}^{CO^2}$	$E_{ads}^{O_2}$	TS1+	TS1−	TS2+	Rate (s^{-1})
Au_{19}/MoS_2-N	−0.69	−0.63	−0.57	0.02	0.36	0.35	1.6
Au_{19}/MoS_2-D	−0.74	−0.56	−0.35	0.13	0.51	0.37	2.2×10^{-1}
Au_{19}/MoS_2-S	−0.67	−0.56	−0.37	0.38	0.57	0.45	4.4×10^{-4}
Au_{19}/MoS_2-DS	−0.77	−0.68	−0.23	0.15	0.53	0.15	3.8×10^{2}

[a] Energy values are given in eV.

Zeng's group found that a decrease in the reaction barrier is the major benefit of the trimolecular mechanism.[68,75] We also found that with the exception of the Au_{19}/MoS_2-S system, there was some decrease in the reaction-energy barrier compared to those of the bimolecular LH mechanism (Table 4). However, in our systems, the most notable advantage of the trimolecular mechanism was the stabilization of the OCOO* intermediate, which increased its lifespan and surface concentration.

Similar to the bimolecular CO oxidation, the reaction rate decreases in the presence of an S vacancy (Au_{19}/MoS_2-D) or under the application of a tensile strain (Au_{19}/MoS_2-S) on the MoS_2 support. However, when both of these coexist (Au_{19}/MoS_2-DS), CO oxidation occurs at the highest reaction rate (3.8×10^2 s^{-1}). Compared to the Au_{19}/MoS_2-D system, which is commonly fabricated in experiments, we expected that a reaction rate increase of three orders of magnitude would be obtained by applying a 5% tensile strain on the support. Additionally, this system exhibited the highest value of $E_{bind}^{Au_{19}}$. This effectively improves the time-dependent stability, which prevents the coalescence of the catalytic Au NPs. Therefore, we suggest that a combinatorial application of a chemical (defect) and a physical (strain) treatment on the supporting MoS_2 is effective for the optimal catalytic activity of the Au_{19}/MoS_2 system.

3.5 CO oxidation at the perimeter near the interface of Au_{19}/MoS_2

The interfacial area at the perimeter of the supported Au NPs and their supporting oxides is regarded as a reactive center for CO oxidation.[4–6] The perimeter can bind and activate an O_2 molecule or become a gateway for the supply of oxygen for CO oxidation by the Mars–van Krevelen mechanism. To verify the plausibility of CO oxidation at the interfacial area in our Au_{19}/MoS_2 systems, we constructed the complete CO oxidation pathway and calculated the rate (Fig. 5 and Table 5). Both CO and O_2 were found to preferentially adsorb on the perimeter of the Au_{19} NPs, that is, the bottom layer instead of on the MoS_2 support, implying that it is difficult for the support to become directly involved in the CO oxidation reaction.

Fig. 5 shows the CO oxidation pathway at the perimeter near the interface, with all the molecular adsorption energies, reaction barriers, and reaction rates shown in Table 5. The CO adsorption energy was slightly higher (0.1–0.2 eV) than that of adsorption on the top layer of the Au_{19} NPs because of steric interaction with the support, which prevents the CO from adopting its most stable adsorption configuration.[76] However, we found that O_2 adsorption at the perimeter is energetically forbidden. Because no Mo atom is exposed on the surface, reactive sites for O_2 adsorption do not exist on the MoS_2 support itself. An exothermic adsorption with a very low $E_{ads}^{O_2}$ of −0.08 eV occurs only for the Au_{19}/MoS_2-N system, while endothermic adsorption occurs in the rest of the systems. Additionally, the reaction barriers for the OCOO* formation in every system are quite high due to the thermodynamic instability of the OCOO* intermediate. The low $E_{ads}^{O_2}$ and the high TS1 activation energy barrier systematically prevent the facile oxidation of CO at the Au_{19}/MoS_2 perimeter. This leads to the low reaction rates presented in Table 5. CO oxidation at the perimeter site of the Au_{19}/MoS_2 is unlikely to occur, regardless of the state of the MoS_2 support.

Table 5 Microkinetic analysis of CO oxidation at the perimeter near the interface between the Au_{19} NP and MoS_2 support[a]

System	E_{ads}^{CO}	$E_{ads}^{O_2}$	TS1	TS1−	TS2	Rate (s^{-1})
Au_{19}/MoS_2-N	−0.57	−0.08	0.3	0.24	0.43	1.7×10^{-3}
Au_{19}/MoS_2-D	−0.52	0.03	0.27	0.12	0.55	3.8×10^{-8}
Au_{19}/MoS_2-S	−0.53	0.18	0.52	0.33	0.40	4.8×10^{-9}
Au_{19}/MoS_2-DS	−0.52	0.05	0.21	0.00	0.51	8.2×10^{-9}

[a] Energy values are given in eV.

4 Conclusions

Herein, we used DFT calculations to study the overall CO oxidation pathway catalyzed by Au_{19} NPs supported on stoichiometric-non-modified MoS_2 and physically or chemically modified MoS_2 supports.

A combination of an S vacancy and a tensile strain was most efficient for the optimization of the reaction pathway and for the achievement of the maximum reaction rate. Of all the tested reaction pathways and reaction centers, the top Au_3 motif of the Au_{19} was found to be reactive for CO oxidation. The perimeter of the Au_{19} NPs and supporting MoS_2 was not able to bind and activate a molecular O_2, confirming that the reaction does not occur at the multi-phase interface in the Au_{19}/MoS_2 systems. The cooperative CO oxidation catalyzed by the Au_3 motif, which incorporates the double CO assisted O_2 activation, assures the highest CO oxidation rate. The chemical stability of the OCOO* reaction intermediate and the activation energy barrier for the final CO_2 production from the OCOO* were the two key controlling factors. The cooperative CO oxidation pathway was especially effective for the stabilization of the OCOO* intermediate.

Our results suggest that the catalytic activity toward the CO oxidation of Au_{19}/MoS_2 can be optimized through a physical or chemical modification of the MoS_2 support. Such modifications also strengthen the binding of the Au_{19} NPs on the MoS_2 support, thus improving the activity and stability of the catalyst at the same time.

Acknowledgements

This research was supported by a National Research Foundation of Korea (NRF) grant funded by the Ministry of Science, ICT & Future Planning (MSIP) (no. NRF-2015R1A5A1037627) and by the NLRL (National Leading Research Laboratory) program of the Korea government (no. 2011-0028612).

Notes and references

1 M. Haruta, N. Yamada, T. Kobayashi and S. Iijima, *J. Catal.*, 1989, **115**, 301–309.
2 M. Valden, X. Lai and D. W. Goodman, *Science*, 1998, **281**, 1647–1650.
3 M. Haruta, *Catal. Today*, 1997, **36**, 153–166.
4 L. M. Molina, M. D. Rasmussen and B. Hammer, *J. Chem. Phys.*, 2004, **120**, 7673–7680.
5 I. X. Green, W. Tang, M. Neurock and J. T. Yates, *Science*, 2011, **333**, 736–739.
6 H. Y. Kim, H. M. Lee and G. Henkelman, *J. Am. Chem. Soc.*, 2012, **134**, 1560–1570.
7 M. Xu, T. Liang, M. Shi and H. Chen, *Chem. Rev.*, 2013, **113**, 3766–3798.
8 M. Chhowalla, H. S. Shin, G. Eda, L.-J. Li, K. P. Loh and H. Zhang, *Nat. Chem.*, 2013, **5**, 263–275.
9 C. N. R. Rao, H. S. S. Ramakrishna Matte and U. Maitra, *Angew. Chem., Int. Ed.*, 2013, **52**, 13162–13185.
10 S. Z. Butler, S. M. Hollen, L. Cao, Y. Cui, J. A. Gupta, H. R. Gutiérrez, T. F. Heinz, S. S. Hong, J. Huang, A. F. Ismach, E. Johnston-Halperin, M. Kuno, V. V. Plashnitsa, R. D. Robinson, R. S. Ruoff, S. Salahuddin, J. Shan, L. Shi, M. G. Spencer, M. Terrones, W. Windl and J. E. Goldberger, *ACS Nano*, 2013, **7**, 2898–2926.
11 G. Du, Z. Guo, S. Wang, R. Zeng, Z. Chen and H. Liu, *Chem. Commun.*, 2010, **46**, 1106–1108.
12 C. Feng, J. Ma, H. Li, R. Zeng, Z. Guo and H. Liu, *Mater. Res. Bull.*, 2009, **44**, 1811–1815.
13 S. Ding, D. Zhang, J. S. Chen and X. W. Lou, *Nanoscale*, 2012, **4**, 95–98.
14 H. Hwang, H. Kim and J. Cho, *Nano Lett.*, 2011, **11**, 4826–4830.
15 Z. Yin, H. Li, H. Li, L. Jiang, Y. Shi, Y. Sun, G. Lu, Q. Zhang, X. Chen and H. Zhang, *ACS Nano*, 2012, **6**, 74–80.
16 H. S. Lee, S.-W. Min, Y.-G. Chang, M. K. Park, T. Nam, H. Kim, J. H. Kim, S. Ryu and S. Im, *Nano Lett.*, 2012, **12**, 3695–3700.
17 W. Choi, M. Y. Cho, A. Konar, J. H. Lee, G.-B. Cha, S. C. Hong, S. Kim, J. Kim, D. Jena, J. Joo and S. Kim, *Adv. Mater.*, 2012, **24**, 5832–5836.
18 B. Radisavljevic, A. Radenovic, J. Brivio, V. Giacometti and A. Kis, *Nat. Nanotechnol.*, 2011, **6**, 147–150.
19 Y. Yoon, K. Ganapathi and S. Salahuddin, *Nano Lett.*, 2011, **11**, 3768–3773.
20 S. Ghatak, A. N. Pal and A. Ghosh, *ACS Nano*, 2011, **5**, 7707–7712.
21 Z. Yin, Z. Zeng, J. Liu, Q. He, P. Chen and H. Zhang, *Small*, 2013, **9**, 727–731.
22 J. Liu, Z. Zeng, X. Cao, G. Lu, L.-H. Wang, Q.-L. Fan, W. Huang and H. Zhang, *Small*, 2012, **8**, 3517–3522.
23 H. Li, Z. Yin, Q. He, H. Li, X. Huang, G. Lu, D. W. H. Fam, A. I. Y. Tok, Q. Zhang and H. Zhang, *Small*, 2012, **8**, 63–67.
24 Q. He, Z. Zeng, Z. Yin, H. Li, S. Wu, X. Huang and H. Zhang, *Small*, 2012, **8**, 2994–2999.
25 B. Hinnemann, P. G. Moses, J. Bonde, K. P. Jørgensen, J. H. Nielsen, S. Horch, I. Chorkendorff and J. K. Nørskov, *J. Am. Chem. Soc.*, 2005, **127**, 5308–5309.
26 T. F. Jaramillo, K. P. Jørgensen, J. Bonde, J. H. Nielsen, S. Horch and I. Chorkendorff, *Science*, 2007, **317**, 100–102.
27 D. Gopalakrishnan, D. Damien and M. M. Shaijumon, *ACS Nano*, 2014, **8**, 5297–5303.
28 L. Liao, J. Zhu, X. Bian, L. Zhu, M. D. Scanlon, H. H. Girault and B. Liu, *Adv. Funct. Mater.*, 2013, **23**, 5326–5333.
29 J. Xie, H. Zhang, S. Li, R. Wang, X. Sun, M. Zhou, J. Zhou, X. W. Lou and Y. Xie, *Adv. Mater.*, 2013, **25**, 5807–5813.
30 A. W. Maijenburg, M. Regis, A. N. Hattori, H. Tanaka, K.-S. Choi and J. E. ten Elshof, *ACS Appl. Mater. Interfaces*, 2014, **6**, 2003–2010.
31 X. Huang, Z. Zeng, S. Bao, M. Wang, X. Qi, Z. Fan and H. Zhang, *Nat. Commun.*, 2013, **4**, 1444.
32 Z. Yin, B. Chen, M. Bosman, X. Cao, J. Chen, B. Zheng and H. Zhang, *Small*, 2014, **10**, 3537–3543.
33 J. Li, W. Tang, H. Yang, Z. Dong, J. Huang, S. Li, J. Wang, J. Jin and J. Ma, *RSC Adv.*, 2014, **4**, 1988–1995.

34 X. Zhong, H. Yang, S. Guo, S. Li, G. Gou, Z. Niu, Z. Dong, Y. Lei, J. Jin, R. Li and J. Ma, *J. Mater. Chem.*, 2012, **22**, 13925–13927.
35 L. Yuwen, F. Xu, B. Xue, Z. Luo, Q. Zhang, B. Bao, S. Su, L. Weng, W. Huang and L. Wang, *Nanoscale*, 2014, **6**, 5762–5769.
36 C. Zhai, M. Zhu, D. Bin, F. Ren, C. Wang, P. Yang and Y. Du, *J. Power Sources*, 2015, **275**, 483–488.
37 T. Li and G. Galli, *J. Phys. Chem. C*, 2007, **111**, 16192–16196.
38 W. S. Yun, S. W. Han, S. C. Hong, I. G. Kim and J. D. Lee, *Phys. Rev. B: Condens. Matter Mater. Phys.*, 2012, **85**, 033305.
39 A. Ramasubramaniam, D. Naveh and E. Towe, *Phys. Rev. B: Condens. Matter Mater. Phys.*, 2011, **84**, 205325.
40 T. Wang, J. Zhuo, Y. Chen, K. Du, P. Papakonstantinou, Z. Zhu, Y. Shao and M. Li, *ChemCatChem*, 2014, **6**, 1877–1881.
41 S. Su, H. Sun, F. Xu, L. Yuwen, C. Fan and L. Wang, *Microchim. Acta*, 2014, **181**, 1497–1503.
42 Z.-R. Xu, J.-L. Luo and K. T. Chuang, *J. Power Sources*, 2009, **188**, 458–462.
43 A. Sanchez, S. Abbet, U. Heiz, W. D. Schneider, H. Häkkinen, R. N. Barnett and U. Landman, *J. Phys. Chem. A*, 1999, **103**, 9573–9578.
44 B. Yoon, H. Häkkinen, U. Landman, A. S. Wörz, J.-M. Antonietti, S. Abbet, K. Judai and U. Heiz, *Science*, 2005, **307**, 403–407.
45 J. Guzman, S. Carrettin and A. Corma, *J. Am. Chem. Soc.*, 2005, **127**, 3286–3287.
46 M. Zhou, A. Zhang, Z. Dai, Y. P. Feng and C. Zhang, *J. Phys. Chem. C*, 2010, **114**, 16541–16546.
47 G. Kresse and J. Hafner, *Phys. Rev. B: Condens. Matter Mater. Phys.*, 1994, **49**, 14251–14269.
48 G. Kresse and J. Furthmüller, *Phys. Rev. B: Condens. Matter Mater. Phys.*, 1996, **54**, 11169–11186.
49 J. P. Perdew, K. Burke and M. Ernzerhof, *Phys. Rev. Lett.*, 1996, **77**, 3865–3868.
50 J. P. Perdew, J. A. Chevary, S. H. Vosko, K. A. Jackson, M. R. Pederson, D. J. Singh and C. Fiolhais, *Phys. Rev. B: Condens. Matter Mater. Phys.*, 1992, **46**, 6671–6687.
51 P. E. Blochl, *Phys. Rev. B: Condens. Matter Mater. Phys.*, 1994, **50**, 17953.
52 G. Henkelman, B. P. Uberuaga and H. Jónsson, *J. Chem. Phys.*, 2000, **113**, 9901–9904.
53 P. Gruene, D. M. Rayner, B. Redlich, A. F. G. van der Meer, J. T. Lyon, G. Meijer and A. Fielicke, *Science*, 2008, **321**, 674–676.
54 S. Bulusu and X. C. Zeng, *J. Chem. Phys.*, 2006, **125**, 154303.
55 C. Xinjun, Y. Guanggeng, W. Andrew Thye Shen and W. Xue-Sen, *Nanotechnology*, 2012, **23**, 375603.
56 Y. Shi, J.-K. Huang, L. Jin, Y.-T. Hsu, S. F. Yu, L.-J. Li and H. Y. Yang, *Sci. Rep.*, 2013, **3**, 1839.
57 C. Du, H. Lin, B. Lin, Z. Ma, T. Hou, J. Tang and Y. Li, *J. Mater. Chem. A*, 2015, **3**, 23113–23119.
58 S. G. Sørensen, H. G. Füchtbauer, A. K. Tuxen, A. S. Walton and J. V. Lauritsen, *ACS Nano*, 2014, **8**, 6788–6796.
59 S. Bertolazzi, J. Brivio and A. Kis, *ACS Nano*, 2011, **5**, 9703–9709.
60 T. Li, *Phys. Rev. B: Condens. Matter Mater. Phys.*, 2012, **85**, 235407.
61 F. Xiaofeng, W. T. Zheng, K. Jer-Lai and J. S. David, *J. Phys.: Condens. Matter*, 2015, **27**, 105401.
62 J.-Y. Noh, H. Kim and Y.-S. Kim, *Phys. Rev. B: Condens. Matter Mater. Phys.*, 2014, **89**, 205417.
63 Y.-C. Lin, D. O. Dumcenco, H.-P. Komsa, Y. Niimi, A. V. Krasheninnikov, Y.-S. Huang and K. Suenaga, *Adv. Mater.*, 2014, **26**, 2857–2861.
64 G. Henkelman, A. Arnaldsson and H. Jónsson, *Comput. Mater. Sci.*, 2006, **36**, 354–360.
65 W. Tang, E. Sanville and G. Henkelman, *J. Phys.: Condens. Matter*, 2009, **21**, 084204.
66 L. Li, Y. Gao, H. Li, Y. Zhao, Y. Pei, Z. Chen and X. C. Zeng, *J. Am. Chem. Soc.*, 2013, **135**, 19336–19346.
67 Y. Gao, N. Shao, Y. Pei, Z. Chen and X. C. Zeng, *ACS Nano*, 2011, **5**, 7818–7829.
68 C. Liu, Y. Tan, S. Lin, H. Li, X. Wu, L. Li, Y. Pei and X. C. Zeng, *J. Am. Chem. Soc.*, 2013, **135**, 2583–2595.
69 B.-T. Teng, J.-J. Lang, X.-D. Wen, C. Zhang, M. Fan and H. G. Harris, *J. Phys. Chem. C*, 2013, **117**, 18986–18993.
70 N. Lopez, T. V. W. Janssens, B. S. Clausen, Y. Xu, M. Mavrikakis, T. Bligaard and J. K. Nørskov, *J. Catal.*, 2004, **223**, 232–235.
71 J. Kim, S. Byun, A. J. Smith, J. Yu and J. Huang, *J. Phys. Chem. Lett.*, 2013, **4**, 1227–1232.
72 T. S. Sreeprasad, P. Nguyen, N. Kim and V. Berry, *Nano Lett.*, 2013, **13**, 4434–4441.
73 H. Sun, J. Chao, X. Zuo, S. Su, X. Liu, L. Yuwen, C. Fan and L. Wang, *RSC Adv.*, 2014, **4**, 27625–27629.
74 S. Su, C. Zhang, L. Yuwen, J. Chao, X. Zuo, X. Liu, C. Song, C. Fan and L. Wang, *ACS Appl. Mater. Interfaces*, 2014, **6**, 18735–18741.
75 P. Wang, X. Tang, J. Tang and Y. Pei, *J. Phys. Chem. C*, 2015, **119**, 10345–10354.
76 L. M. Molina and B. Hammer, *Phys. Rev. Lett.*, 2003, **90**, 206102.